Good's Buffer Based Highly Biocompatible Ionic Liquid Modified PLGA Nanoparticles for the Selective Uptake in Cancer Cells

Gagandeep Singh,[a] Gaya S. Dasanayake,[a] Claylee M. Chism,[a] Priyavrat Vashisth,[a] Amandeep Kaur,[a] Sandeep Kumar Misra,[b] Joshua S. Sharp,[b] Eden E. L. Tanner*[a]

[a] *Department of Chemistry and Biochemistry, University of Mississippi, University, MS 38677*
[b] *Department of BioMolecular Sciences, University of Mississippi, University, MS 38677*

*Address for correspondence:
Dr. Eden E. L. Tanner
Department of Chemistry & Biochemistry
The University of Mississippi
University, MS 38677, United States
Email: eetanner@olemiss.edu
Phone: 662-915-1165

Abstract. Achieving safe and efficacious drug delivery is still an outstanding challenge. Herein we have synthesized 20 biocompatible Good's buffer-based ionic liquids (GBILs) with a range of attractive properties for drug delivery applications. The synthesized GBILs were used to coat the surface of poly (lactic-co-glycolic acid) (PLGA) by nanoprecipitation-sonication and characterized by dynamic light scattering (DLS) and proton nuclear magnetic resonance (^{1}H NMR) spectroscopy. The GBIL-modified PLGA NPs were then tested for their interaction with bio-interfaces such as serum proteins (using SDS-PAGE and LCMS) and red blood cells (RBCs) isolated from human and BALB/c mouse blood. In this report, we show that surface modification of PLGA with certain GBILs led to modulation of preferential cellular uptake towards human triple-negative breast cancer cells (MDA-MB-231) compared to human normal healthy breast cells (MCF-10A). For example, cholinium N, N-bis(2-hydroxyethyl)-2-aminoethane sulfonate (CBES) coated PLGA NPs were found to be selective for MDA-MB-231 cells (60.7 ± 0.7 %) as compared to MCF-10A cells (27.3 ± 0.7 %). In this way, GBIL-coatings have increased PLGA NP uptake in the cancer cells by 2-fold while decreasing the uptake towards normal healthy breast cells. Therefore, GBIL-modified nanoparticles could be a versatile platform for targeted drug delivery and gene therapy applications, as their surface properties can be tailored to interact with specific cell receptors and enhance cellular uptake. This formulation technique has shown promising results for targeting specific cells, which could be explored further for other cell types to achieve site-specific and efficient delivery of therapeutic agents.

1. Introduction. Cancer affects millions of people every year, with an estimated 19.3 million new cases and 10.0 million deaths worldwide in 2020.[1] The available treatments for cancer vary depending on the type and stage of the disease but commonly include surgical procedures, radiation therapy, and chemotherapy.[1] For instance, triple-negative breast cancer (TNBC), which accounts for 10-15% of breast cancer cases, is characterized by the lack of expression of progesterone receptor (PR), estrogen receptor (ER), and human growth factor receptors 2 (HER-2).[2] The high relapse rate, molecular heterogeneity, and risk of metastasis towards different organs (such as lung, liver, bone, and lymph nodes) make it one of the most aggressive and complex clinical subtypes of breast cancer encountered worldwide. Furthermore, the absence of hormone receptors prevents the use of endocrine therapy (hormone targeting) and thus bound to rely on chemotherapy for the treatment, which lacks specificity, causes high toxicity, organ damage, poor response rates, and develops multidrug resistance (MDR) over time.[3-6] TNBC disproportionally impacts Black and African American women, who are three-fold more likely to receive a diagnosis of TNBC than white women diagnosed with breast cancer.[7] Therefore, urgent innovative drug delivery modalities are require to overcome these challenges.

Over the past few decades, nanotechnology has emerged as a promising platform for the selective identification and targeted delivery of chemotherapeutic drugs.[8-11] Among different nanocarriers,[12] polymer-based nanoparticles (NPs) are extensively explored drug delivery systems due to their versatile design, biocompatibility, and ability to encapsulate a wide range of drugs with improved solubility and stability.[13-15] Due to their submicron size, NPs can easily penetrate through biological barriers such as inflammatory zones, tumor microcapillaries, and epithelium (e.g., liver and intestinal tract) and thus get efficiently absorbed by different cell types.[10, 11] After accumulating at the targeted site, the nanoparticle drug reservoir provides a continuous supply of the desired therapeutic at the disease/tumor site. It can thus effectively treat the disease condition. However, in practice, from research to clinical translation, nanomedicines encounter many challenges, which include the rapid clearance by the immune system, heterogeneity of tumor targets, and manufacturing scalability (rapid, precise, and reproducible synthesis of NP).[16, 17] To address these issues, recently our group has developed relatively facile ionic liquid-modified polymer NP formulations, minimizing opsonization and extended blood circulation time along with organ-specific targeting.[18]

Ionic liquids (ILs) are a class of low melting (< 100 °C) organic salts comprised of asymmetric anion-cation combinations. ILs hold excellent physicochemical properties such as high thermal stability, solvation capacity, low volatility, and non-flammability, leading to their functionality in diverse fields of applications.[19] The inherent richness of complex architectures of chemical forces and the ability to precisely engineer these interactions by altering the cation/anion components of IL enables us to achieve controlled nanoscale self-assembly of ionic motifs.[20] Apart from the above mentioned properties, the high safety profiles (toxicity and biodegradability) of ILs are the primary prerequisite for their use in biological applications.[21-23] Therefore, in this regard, in the recent past many bio-inspired ILs (BILs) have been developed and demonstrated to their utilization for various biological applications.[24-28]

Herein, we have synthesized and characterized 20 Good's buffer-based ionic liquids (GBILs), which were investigated for their cytotoxicity against MCF-10A cells at various concentrations. The high biocompatibility of GBILs motivated the assembly of GBIL-modified

PLGA NPs via nanoprecipitation-sonication , followed by their characterization using dynamic light scattering (DLS) and nuclear magnetic resonance (NMR) spectroscopy. The prepared GBIL-NPs were found to be stable for 50 days at 4 C. The interactions of GBIL-NPs at various bio-interfaces were explored using human and mouse serum adsorption studies using SDS-PAGE and LCMS, with red blood cells (RBCs) in hemolysis experiments, and cellular uptake of GBIL-modified NPs in MCF-10A and MDA-MB-231 cell lines. The experimental findings revealed that the internalization of GBIL-NPs was dependent on the GBIL structure, which was observed in both cell types. Therefore, the use of versatile combinations of IL cations and anions, along with IL-modified polymer formulation techniques, renders this approach highly promising for targeting various other types of cells, warranting further exploration.

2. Experimental.

2.1. Materials. Starting materials for the synthesis of Good's buffers were procured from Sigma-Aldrich. Brief details about the reactants are as follows: choline bicarbonate (80% in H_2O, #C7519-500 mL); N, N-Bis(2-hydroxyethyl) glycine (Bicine, ≥99 %, #B3876-100G); N, N-Bis(2-hydroxyethyl)-2-aminoethanesulfonic acid (BES, ≥99.0 %, #B9879-25G); 3-(N,N-Bis[2-hydroxyethyl] amino)-2-hydroxypropanesulfonic acid (DIPSO, ≥98.0 %, #D0306-25G); N-(2-Acetamido) iminodiacetic acid (ADA, ≥99.0%, #00307-25G); N-[Tris(hydroxymethyl) methyl] glycine (Tricine, ≥99%, #T0377-100G); 2-[(2-Hydroxy-1,1- is (hydroxymethyl)ethyl) amino] ethane sulfonic acid (TES, ≥ 99 %, #T1375-500G); 2-Hydroxy-1,1-bis(hydroxymethyl) ethyl) amino]-1-propanesulfonic acid (TAPS, ≥99.5%, #T5130-100G); 2-Hydroxy-3-[tris(hydroxymethyl) methylamino]-1-propanesulfonic acid (TAPSO, ≥99%, #T9269-100G); N-(2-Acetamido)-2-aminoethanesulfonic acid (ACES, ≥ 99.0%, #A9758-25G); 4-(2-Hydroxyethyl) piperazine-1-ethanesulfonic acid (HEPES , ≥ 99.5%, #H3375-100G); 4-(2-Hydroxyethyl) piperazine-1-propanesulfonic acid (EPPS, ≥ 99.5%, #E9502-10G); 2-Hydroxy-3-(4-(2-hydroxyethyl) piperazin-1-yl) propane-1-sulfonic acid (HEPPSO, #R426725-1G); N-(2-Hydroxyethyl) piperazine-N′-(4-butanesulfonic acid) (HEPBS, ≥99%, #H6903-25G); 2-(Cyclohexyl amino) ethane sulfonic acid (CHES, ≥ 99.0%, #C2885-100G); 3-(Cyclohexyl amino)-1-propane sulfonic acid (CAPS, ≥ 99%, #C2632-100G); 3-(Cyclohexyl amino)-2-hydroxy-1-propane sulfonic acid (CAPSO, ≥ 99% anhydrous basis, #C2278-100G); 2-(N-morpholino) ethane sulfonic acid (MES, ≥ 99%, #M3671-50G); 3-(N-Morpholino) propane sulfonic acid (MOPS, ≥ 99.5%, #M1254-250G); Piperazine-1,4-bis(2-hydroxypropanesulfonic acid) dihydrate (POPSO, ≥ 99%, #P3405-25G); 1,4-Piperazinediethanesulfonic acid (PIPES, ≥99%, #P6757-100G). Poly (D, L-lactide-co-glycolide) carboxylic acid-terminated, average Mw 38,000-54,000, lactide: glycolide 50:50, (#719900-5G, Resomer 504H); Deuterium oxide (#435767-1KG); acetonitrile (HPLC-Grade, #34851-4L); Sodium 2,2-dimethyl-2- silapentane-5-sulfonate-D6 (DSS, #DLM-32-1) internal standard for quantification using NMR was obtained from Cambridge Isotope Laboratories. Ultrapure MilliQ water was obtained from Millipore MilliQ purifier (#Milli-Q IQ 7000). Molecular Probes DiD' solid, far-red dye, (1,1'-dioctadecyl-3,3,3',3'-tetramethylindodicarbocyanine, 4-chlorobenzene sulfonate salt) (#D7757-10mg) was procured from Thermo Fisher Scientific. Amicon-4 mL 30 kDa MWCO ultracentrifugation filter tubes were purchased from Sigma Aldrich (Ultra-4, #UFC803096). COSTAR 96-well opaque black-bottom and 96-well clear plates (#353075) were obtained from Corning. 6-well polystyrene tissue culture treated multiple well plates (#229106) obtained from

Celltreat. DMEM/High glucose without sodium pyruvate and L-glutamine cell culture solution (#SH30081.FS), Dulbecco's Phosphate Buffered Saline (DPBS), Sterile, 7.0 - 7.6, without calcium and magnesium, liquid (#SH30028.02), and trypsin-EDTA (#SH30042.01) were obtained from the Cytiva life sciences. Penicillin-streptomycin (#P4458-100ML), Fetal bovine serum (FBS, #F0926-500ML), and Cholera toxin from Vibrio cholerae, $\geq 90\%$ (SDS-PAGE), lyophilized powder (#C8052-1MG) were purchased from Sigma Aldrich. Mammary Epithelial Cell Growth Medium (MEGM) BulletKit (CC-3151 & CC-4136, #CC-3150) was purchased from Lonza. CellTiter-Glo Luminescent cell viability assay (#G7570) was purchased from Promega Corporation. The MCF-10A and MDA-MB-231 cell lines were obtained from ATCC. MCF-10A cell line was cultured in MEGM medium supplemented with 10% v/v FBS, 100 ng/mL cholera toxin, 1% penicillin-streptomycin (penstrep), 20 ng/mL epidermal growth factor, 500 ng/mL hydrocortisone, 5% Chelex-treated horse serum, and 0.01 mg/mL human insulin. MDA-MB 231 cell line was cultured in DMEM with 1% penicillin-streptomycin and 10% v/v FBS. RAPIDstain™ Reagent (#553215-1L, Sigma-Aldrich), DAPI (#23002, Biotium, EverBrite™ Mounting Medium with DAPI, Size=10 mL), paraformaldehyde (PFA, 16% aqueous solution, #15710-S), CellBrite® (#30021, Biotium), human serum (lyophilized power, #D314-05) and mouse serum (lyophilized power, D308-05) from Rockland. Human blood and mouse blood was obtained from Bio-IVT and used with approval of the University of Mississippi Biosafety Committee.

2.2. Methods.

2.2.1. Preparation of good's buffer-based ionic liquids (GBILs). GBILs comprised of a choline cation and one of 20 Good's buffer anions were synthesized using acid-base neutralization reaction in a molar ratio 1:1 (except CADA, CPOPSO, and CPIPES, which were made at a cation: anion ratio of 2:1) as described fully elsewhere.[29] The synthesis procedure for the GBILs is described in detail result and discussion section.

2.2.2. Preparation of bare PLGA NPs and GBIL-coated NPs. PLGA polymer was dissolved in HPLC-grade acetonitrile (ACN) (organic phase) at 1 mg mL^{-1} and vortexed for 3 mins to ensure complete mixing. Then the described organic phase (1mg ml^{-1} PLGA solution) was added dropwise in 1 min with a Pasteur pipette to aqueous phase 3 mL MilliQ water (or 3 mL D_2O for ^1H NMR samples) in a glass scintillation vial, which was stirred at 1200 rpm at room temperature for 3 h. For cell uptake experiments, far-red fluorescent dye DiD was encapsulated in PLGA NPs. These NPs were made by dissolving PLGA and far-red fluorescent DiD dye in HPLC-grade ACN (organic phase) separately at 1 mg mL^{-1} and vortexing for 3 mins to ensure complete mixing. The far-red fluorescent DiD dye solution was then added to the PLGA solution to make 1% DiD of PLGA by mass as organic phase. Then, the organic phase (1% DiD by mass in 1 mg ml^{-1} PLGA solution) was added dropwise using a Pasteur pipette to the aqueous phase (3 mL MilliQ water) while stirring at 1200 rpm at ambient temperature for 3 h in a glass vial. Assembled PLGA NPs were then filtered using a 30 kDa MWCO centrifuge filter at 2500 rpm for 1 h at 4 ^{o}C and brought up to 1 mg ml^{-1} with MQ water or 1x PBS buffer depending upon their desired application. For making GBIL-coated NPs, 30 mg of each GBIL was dissolved in 50μL MQ water which was added dropwise to the premade PLGA NPs (made by nanoprecipitation method as described above) while sonication in a bath-sonicator for 10 minutes at 25 ^{o}C.

2.2.3. Nuclear Magnetic Resonance (NMR) spectroscopy. GBILs and GBIL-coated PLGA NPs characterization by ^{1}H NMR spectroscopy was performed on a Bruker Ascend 400 MHz. For the quantification of GBIL-coated PLGA NPs, 10 uL of DSS (stock concentration 0.2 mg ml^{-1} in D_2O) was added to filtered 500 uL GBIL-PLGA NPs solution prepared in D_2O. The proton peak of DSS at 0 ppm was normalized to 9 protons and then compared to the signals from the choline cation and GBILs anion, the original signal from the neat IL, the moles of DSS (8.919×10^{-7} mol), and the quantity of NPs in a 1 mg/mL solution (5×10^{13} NPs) were taken into consideration to calculate the amount of GBIL coated over the PLGA NPs (Table 1).

2.2.4. Cytotoxicity. The invitro cytotoxicity of GBILs was determined using MCF-10A cell lines. The MCF-10A cells were cultured on cell culture-treated 96-well plates at 1.5×10^4 cell density per well) under standard conditions (incubation at 37 C and 5% CO_2, MEGM media supplemented with 10% FBS, 1% penicillin-streptomycin, 100 ng mL^{-1} cholera toxin and growth hormone). At ~70 % confluency the cells were treated with different concentration (0.02 mmolL^{-1} to 150 mmolL^{-1}) of GBILs and then incubated for 24 h. After 24 h, the cell media containing excess/free GBIL was replaced by 100 uL of new media and 100 uL CellTiter-Glo(R) luminescent cell viability reagent was added to each well. The prepared 96-well plate was incubated at 37 ^{o}C for 15 mins and then read for luminescence at microplate reader (Biotek H1 Synergy Hybrid Multi-mode). The percentage cell viability was calculated against the negative control.

2.2.5. Dynamic Light Scattering (DLS). The changes in the hydrodynamic diameter (D_h) and zeta potential (surface charge) of PLGA NPs before and after GBIL coating was monitored using Zetasizer Pro, NanoZS (from Malvern Instruments, UK) equipped with a He-Ne laser (with avalanche photodiode detector QE > 50 % 633 nm, 4mW) having in-built temperature controller. The data was recorded at scattering angle of 173° to the incident beam in polystyrene cuvette (DTS0012 cuvette, #D-51588) at 25 C with a fluorescent filter turned on. The measurements were performed in triplicates, and each reading was averaged from 15 internal runs. Zeta potential measurements was performed using a disposable zeta cell (DTS1070) on the same NP solution sample. The DLS samples were prepared by diluting 100 uL of filtered NPs solution with 900 uL of MilliQ water.

2.2.6. Hemolysis. Hemolysis was performed following a previously published protocol.[18] Briefly, red blood cells (RBC) from commercially available human and mouse (BALB/c) whole blood were isolated and washed with saline. Isolated RBCs were then diluted to 1:50 with saline to create an RBC stock which was then treated in the ratio 190 uL, 180 uL and 160 uL of RBC to 10 uL, 20 uL, and 40 uL of bare PLGA and GBIL-PLGA NPs (1 mg mL^{-1} in 1x PBS) i.e., 1:5, 1:10, and 1:20 of RBCs to NPs respectively in quadruplicate in a 96-clear well plate. The prepared 96-plate was incubated at 37 ^{o}C for 1 h, then 200 uL volume from each well was transferred to 1.5 mL plastic tube and centrifuged at 4°C at 500*g* for 10 min. 100 uL supernatant was collected from each tube to measure absorbance at 405 nm with UV-vis using microplate reader. 20% Triton-X-100 and 1 x PBS pH 7.4 were used as positive and negative control under the same conditions of treatment. The percentage hemolysis was calculated by subtracting the negative control (1 x PBS, i.e., minimum baseline) from each absorbance value and then normalizing against the positive control (20% Triton-X-100).

2.2.7. Serum protein adsorption (a) SDS-PAGE study. The serum protein adsorption study was performed in accordance with the previously reported protocol with slight modifications.[18] The bare PLGA NPs and GBIL-PLGA NPs were mixed and incubated in whole human or mouse serum separately in 1:4 ratio (100 µL NPs: 400 µL serum) in 1.5 mL centrifuge tubes and incubated at 37 °C for 30 min on a shaker (VWR orbital shaker Mini, Cat #NO12620938). The neat serum-treated NP samples were centrifuge-washed three times with 1 x PBS for 15 min at 3000 rpm. After each wash, the non-adsorbed serum phase (400 µL of supernatant) was removed carefully and replaced by an equivalent amount of fresh 1 x PBS. The remaining ~100 µL liquid with NP-protein pellet was mixed gently with new 1 x PBS (400 µL) and centrifuged. After the final centrifugation, ~50 µL infranatant of each sample was transferred to a new centrifuge tube. Lamelli buffer was added to each sample in 1:1 ratio and incubated at 100°C for 5 min. The prepared samples were then loaded (15 µL) along with a ladder (rainbow ladder for mouse serum and Page ruler for human serum studies) to an SDS-PAGE (12% tris-Gly-SDS running buffer, Bio-Rad) system and run for 50 min at 150 V. The gel was washed thrice with 150 mL MQ water for 10 mins. After removing the water, the gel was covered with 50 mL of rapid stain and shaken for 1 h. After 1 h, the staining solution was removed, and the gel was washed with MQ water twice followed by the addition of 200 mL MQ water, and allowed to stand for 30 mins or more at room temperature until the bands were clearly visible.

(b) Liquid Chromatography-Tandem Mass Spectrometry (LC-MS/MS) Analysis. To determine the affinity of various blood serum proteins to GBIL-PLGA NPs, the identities and relative amounts of serum proteins (in human and mouse serum) were determined by LC-MS/MS. The LC-MS samples were prepared by mixing bare PLGA NPs and GBIL-PLGA NPs in 1:1 ratio (i.e., 100 µL NPs: 100 µL serum) for 30 minutes at 37 °C with constant shaking. The negative control (i.e., serum only) sample was prepared by mixing 100 µL 1 x PBS: 100 µL serum and incubated under same condition as mentioned above. After incubation, all samples were centrifuged three times at 3000 rpm for 15 min at 4 °C. In each centrifugation step, 100 µL of supernatant (unabsorbed serum) was removed carefully and replaced with fresh 1xPBS and mixed gently. The final centrifugation wash was done at 4500 rpm for 10 minutes at 4 °C.

The protein was collected and a final concentration of 50 mM Tris, 1 mM $CaCl_2$, 0.1% Rapigest (Waters) was added. The samples were incubated at 60 °C for 30 min and cooled. Reduction and thiol alkylation was performed with 10 mM DTT and 20 mM iodoacetamide in the dark. Sequencing-grade modified trypsin (Promega) at 1:20 ratio of protease: protein was added and incubated overnight with rotation at 37 °C. Formic acid was added to a final concentration of 0.1% and the samples were run on Exploris 240 Orbitrap mass Spectrometer (Thermo Scientific). The samples were loaded onto an Acclaim PepMap 100 C18 nanocolumn (0.075 mm × 150 mm, 2 µm, Thermo Fisher Scientific). Peptides were separated on the chromatographic system using mobile phase A (0.1% formic acid in water) and mobile phase B (0.1% formic acid in acetonitrile) at a flow rate of 300 nL/min. The peptides were eluted with a gradient consisting of 2 to 32% solvent B over 23 min, ramped to 95% solvent B over 5 min, held for 4 min, and then returned to 2% solvent B over 3 min and held for 8 min. All data were acquired in positive ion mode. The spray voltage was set to 2450 V, and the ion transfer tube was set to 300 °C. The

MS data were collected with a resolution of 60000 with a scan range of 250-2000 m/z. In CID MS/MS mode, full MS scans were followed by eight subsequent MS/MS scans on the top eight most-abundant peptide ions. Collision energy was set to 30%. Precursor *m/z* was excluded after selection for MS/MS five times, with an exclusion duration of 12 seconds. The data was searched by proteomics search engine Byonic V.4.4.2 (Protein Metrics, San Carlos, CA). False discovery rate was set to 1% at the protein level. The proteins with log probability <5.0 were discarded and only proteins with at least 2 peptides were included. The intensity of the common trypsin autolysis products was used to digest the protein samples were used for normalization of the relative abundance of the protein. To calculate the relative amount of the protein in that sample, first the intensity of a particular protein was divided by the intensity of trypsin in that particular sample. Then, the same value was obtained from the serum control for the same protein. Finally, the values for the protein from samples were divided by the values obtained from serum control and converted to log10.

2.2.7. Fluorescence-activated cell sorting (FACS). For cellular uptake experiments, MCF-10A (in MEBM media with 10 % FBS, 1% pencillin-streptomycin, cholera toxin and supplements) and MDA-MB-231 cells (in DMEM with 10% FBS and 1% penicillin-streptomycin) were cultured in cell culture-treated 6 well plates at 3 x 10^5 cell density per well. At ~80 % confluency, the respective media was replaced with new media, and each cell type was treated with 10, 30, and 50 µg mL^{-1} of GBIL-coated DiD encapsulated PLGA NPs, along with untreated cell-only samples as a negative control, followed by incubation at 37 °C for 12 h. After 12 h, the media was removed, and cells were washed twice with DPBS buffer. 150 µL of Trypsin-EDTA was added in each well to detach cells, neutralized with 5 % FBS buffer solution, and collected in 1.5 mL centrifuge tubes for FACS analysis. The qualitative FACS measurements were performed on Attune NxT acoustic focusing cytometer (Model #AFC2) with gating for live cell population scatter *vs.* far-red fluorescence (APC). The quantitative analysis for the amount of DiD present in the cells. Thus, NPs at different concentrations of GBIL-coated DiD encapsulated PLGA NPs, the same cell samples were run on microplate reader (Biotek H1 Synergy Hybrid Multi-mode) at λ_{ex} 640 nm/ λ_{em} 670 nm.

2.2.8. Confocal Microscopy: For confocal imaging, both MDA-MD-231 and MCF 10A cells were grown on µ-slide 8 well with 2.5 x 10^5 cells per well in DMEM-F12 and MEGM respectively) at standard conditions (incubation at 37 °C and 5% CO_2). At ~80 % confluency the cells were treated with CBES coated PLGA encapsulated DiD NPs and bare PLGA NPs at 10, 30 and 50 µg mL^{-1} respectively. The treated cells were then washed and stained for nuclei with DAPI and cytoplasmic membrane dye CellBrite™ Green (5 µL bright green mixed in 3 ml of fresh cell media), following cell fixation with 4% paraformaldehyde solution. After the fixation, coverslips were mounted on microscope slides for imaging. All images were taken using a confocal Leica SP8X under a 63× oil immersion lens.

2.2.9. Statistical Analysis. The statistical analysis of the data was performed in Microsoft Excel 2019. All the data presented in the paper is represented as mean value ± standard deviation of three independent experiments. A two-tailed critical student's t-test was used to compare the two groups.

3. Results and Discussion.

3.1. Synthesis and characterization of good's buffer-based ionic liquids (GBILs). The rationale for choosing these molecular structures for synthesizing GBILs lies in their evident biocompatibility and biological resemblance. This rationale was extended to encompass various alkyl chain lengths and combinations of functional groups within the same GB anion structure. Biocompatibility ensures that the IL components won't trigger adverse reactions in biological systems, while biological resemblance amplifies the IL's capacity to engage with cellular components and, consequently, regulate its selective uptake through the cell membrane. By mimicking natural compounds, ILs can harness existing cellular pathways and receptors, facilitating their intended biological effects. To better comprehend the relationship between molecular properties and structure, the 20 GBILs were classified into four categories based on their distinct molecular structures (Figure 1). For the sake of simplicity, throughout the manuscript, choline is abbreviated as 'C' when referring to GBILs. For instance, 'Choline Tricine' is abbreviated as 'CTricine.

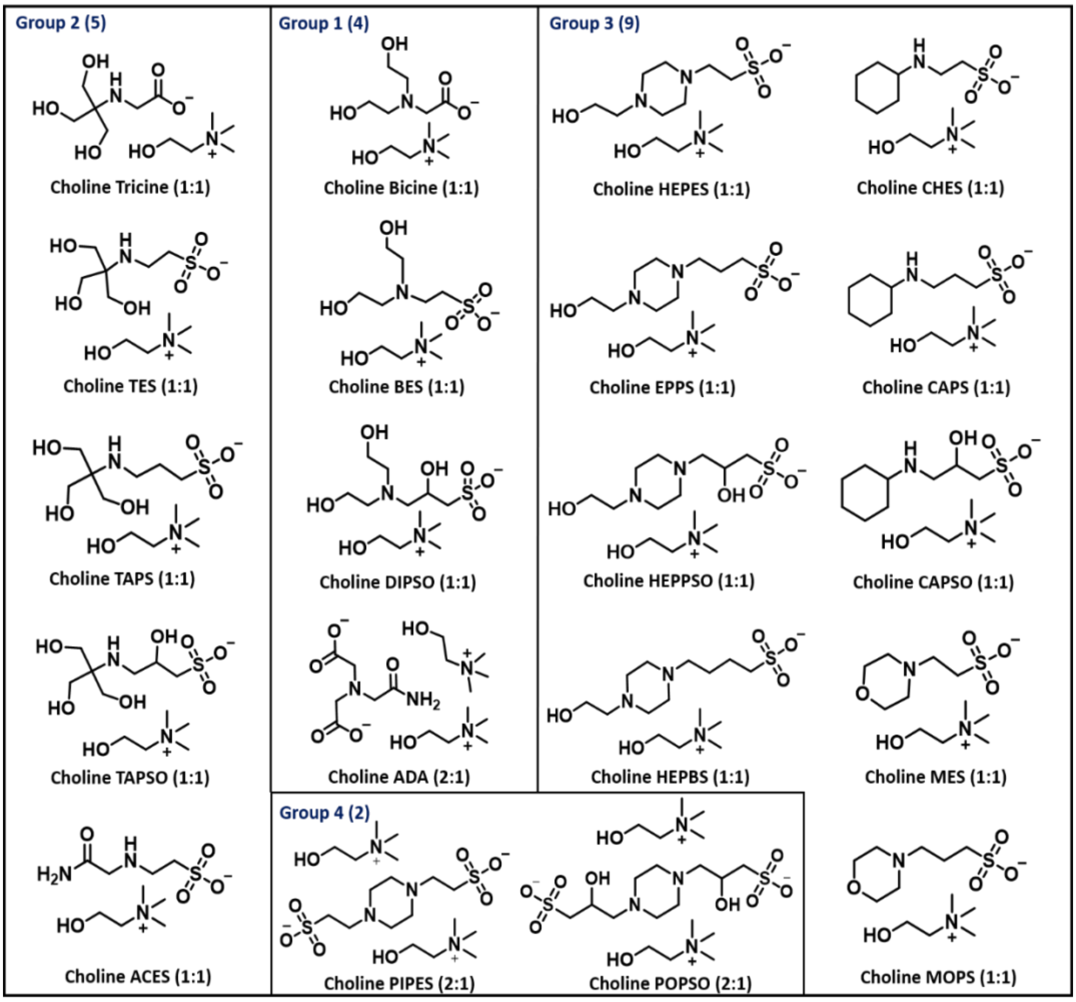

Figure 1: Molecular structures of the good's buffer-based ionic liquids (GBILs) synthesized in this study.

In brief, choline bicarbonate was added dropwise to a slight molar excess of Good's buffer anion while constant stirring in aqueous media at 50 °C for 12 h. The solvent was evaporated under reduced pressure at 60 °C yielding a yellowish to transparent viscous liquid. To remove the unreacted buffer, the obtained liquid was mixed with acetonitrile and methanol (1:1 v/v) for 1 h to precipitate the excess buffer. The precipitated contents were filtered, and the recovered solution was dried under reduced pressure at 60 °C. The GBIL was stored in a vacuum oven for 48 hours at 60 °C at -40 mmHg (relative to atmospheric pressure) to remove residual water. The water content of each GBIL was found to be less than 0.1 wt % by Karl Fisher titration. The detailed proton NMR characterization of all GBILs is provided in the supporting information.

3.2. Cytotoxicity Evaluation of GBILs. To explore possible biomedical applications of the synthesized GBILs, it is required to investigate their biological compatibility towards the human body at the cellular level. In this regard, cytotoxicity studies were conducted on a human mammalian cell line, MCF-10A, for 20 GBILs at a concentration range of 0.02 mmol L^{-1} to 150 mmol L^{-1} (Figure 2 and Figure S1). For comparison, the cell viability profile of GBILs is shown at 8, 16, 32, 64, 100, and 150 mmolL^{-1} with the complete cytotoxicity studies in the Figure S1.

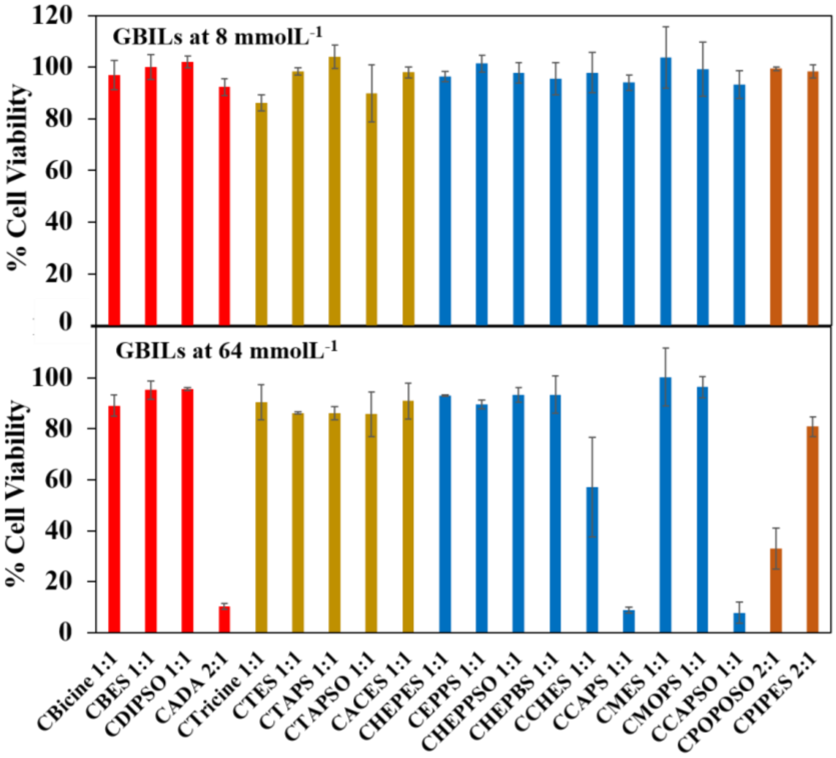

Figure 2. Cytotoxicity profile showing high biocompatibility of GBILs towards MCF-10A cell line. (A) At 8 mmol $L^{-1}$and (B) At 64 mmol L^{-1} of GBILs. Different colors of the bars in the graph signify GBILs classified in different groups to understand the cytotoxicity (n = 3) dependency on the molecular structure of GBILs.

Interestingly, all GBILs were found to be non-toxic towards MCF-10A cells at 8 mmol L^{-1} (Figure 2). At 16 mmol L^{-1}, the cell viability in the case of CADA, CCAPS, and CCAPSO drops to 86.7 ± 3.5 %, 79.1 ± 2.7 %, and 70.8 ± 5.5 %, respectively (Figure S1). The same GBILs become relatively more cytotoxic at 32 mmol L^{-1} and 64 mmol L^{-1} wherein the cell viability falls below 20 %. At 64 mmol L^{-1}, CCHES and CPOPSO show more significant toxicity, but 15 out of 20 GBILs retain high biocompatibility towards MCF-10A cells. On reaching concentration of 100 mmol L^{-1}, 4 out of 20 GBILs i.e., CMES (94.7 ± 10.0 %), CBES (81.4 ± 4.5 %), ACES (80.4 ± 5.2%) and CMOPS (75.3 ± 2.5%) were observed to maintain high cell viability. In contrast, other GBILs showed variable degrees of cytotoxicity. Finally, at 150 mmol L^{-1} only CMES was found to show cell viability more than 50 % (53.6 ± 6.4 %). It is difficult to comprehend the cellular toxicity trend as a function of the molecular structures of GBILs at this point. However, the relatively low cytotoxicity of GBILs towards MCF-10A could be attributed to the favorable molecular interactions of GB anions in the biological environment, particularly: (a) maintaining compatible pH, which is critical for the survival of cells (and thus minimizing potential toxicity)[30], (b) the fact that GB anions have been reported to possess antioxidant and anti-inflammatory properties[31], and (c) the fact that the anions show structural similarity with certain cell substrates such as amino acids, e.g., Tricine and Bicine (Figure 1) are N-substituted derivatives of glycine. These features of GB anions might allow them to interact with the cellular components in a less disruptive way, making these ILs relatively more biocompatible compared to other classes of ILs.[32]

It is important to note that the cytotoxicity of the investigated GBILs were found to be very low as compared to earlier reported ILs[33] (except N-succinyl-DL-alaninate, $IC_{50} > 500$ $mmolL^{-1}$ towards normal human dermal fibroblasts[34]). The cytotoxicity of previously published ILs with different cation-anion combinations has been conducted on different cells lines, such as IPC-81,[35] Hela,[36] MCF-7,[37, 38] C6 Glioma,[35, 39] MRC-5,[40] Huh-7,[40] HEK[40] , HT-29,[41] CaCo-2[41, 42] and HDFn[34] in different concentration ranges. The low EC_{50} values of these ILs were assigned to the length of incubation time, lipophilicity (i.e., alkyl chain length, aliphatic/aromatic groups) of either anion or cation and presence of hydrolysable groups[43] (e.g., BF_4) in ILs.[33] On the other hand, another set of ILs comprising bioderived ingredients or appended hydroxy/ ether functionality in IL ions, such as choline amino acids have also been synthesized and tested for their biocompatibility. However, the nature of the anion conjugated with the bio-ion (choline/ amino acid as cation or anion) was found to strongly affect the IL toxicity[34, 44] and their biophysical interaction with different enzymes/proteins[45-48]. Therefore, it is recommended to explore bio-derived alternatives for both cations and anions to design bio-ILs with desired chemical properties.

3.3. Characterization of GBIL-PLGA NPs. The robust biocompatibility of GBILs motivated us to explore the GBILs as the coating material for PLGA nanoparticles, an FDA-approved polymer for drug delivery applications. The bare PLGA NPs were assembled using nanoprecipitation from acetonitrile, followed by the addition of ILs while sonicating in a water bath (see Methods Section for details). The dynamic light scattering (DLS) measurement shows an increase in the average hydrodynamic diameter (D_h) of the PLGA NPs from 50.6 ± 0.3 nm to 260 ± 3 nm (except CTAPSO, which measured larger at 515 ± 7 nm) after surface modification by GBILs (Table S1). In most cases, the polydispersity index (PDI) of GBIL-PLGA NPs remains at ≈ 0.1, indicating a uniform size distribution of the NPs after surface modification (Figure 3, dots). The shift in surface charge of PLGA NPs (-26 ± 3 mV) towards a more negative surface charge after GBIL (up to -54 ± 1 mV, Figure 3B) addition is indicative of electrostatically driven self-assembly of GBIL ions onto the NP, with the negative charge indicating that the GB anions comprise the outermost layer, meaning that the GB anion is more available to interact with biological interfaces similar to the carboxylate acid-based IL coated polymer NPs.[18, 49] The synthesized GBIL-PLGA NPs were found to be stable up to 50 days at 4 °C (Figure S2) indicating their relatively greater stability as compared to other reported IL-NP systems.[49]

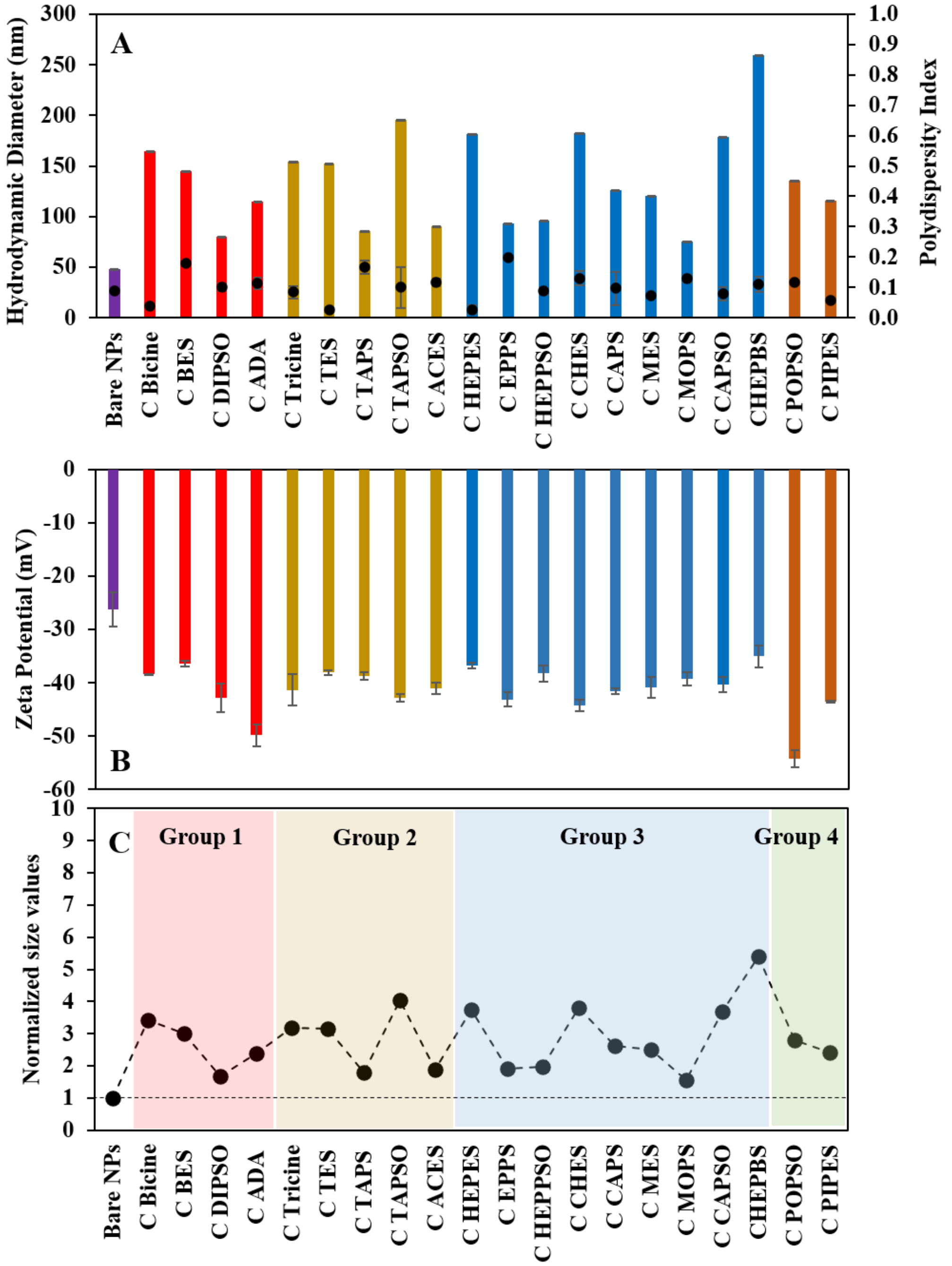

Figure 3. Good's buffer-based ionic liquids are successfully able to coat PLGA nanoparticles. DLS profile of different GBILs (A) Hydrodynamic diameter (colored bars) and Polydispersity index (black dots); (B) Zeta potential profile (black bars); (C) Size plot normalized with respect to PLGA NPs (n = 3).

The comparative D_h and zeta potential profile of GBIL-PLGA NPs indicates a 2 to 3 times increase in size and 1.5 to 2 times decrease in surface charge (negative potential) as compared to bare PLGA NPs. It is assumed that during the addition of GBILs to the premade PLGA NPs, the GBIL ions get sufficient time to self-assemble in their most stable thermodynamic state on the surface of PLGA NPs. This assertion is also supported by the consistency in the hydrodynamic diameter of GBIL-PLGA NPs as the function of time (Figure S2). Therefore, the relative extent of the increase in size and charge could be attributed to the structural differences in GBILs, particularly differences in the GB anions, since the choline cation was held constant to simplify the normalized size plot was plotted by dividing the size of all GBIL-PLGA NPs by the size of PLGA NPs (48.2 ± 0.7 nm) (Figure 3C).

In Group 1, CBicine-coated PLGA NPs were found to be the largest, followed by CBES-NPs, CADA-NPs, and CDIPSO-NPs. A similar trend has also been observed in the quantitative NMR profile of GBIL-NPs, where the amount of these GBILs per NP of PLGA was found to be highest for CBicine (3-fold higher than that of CDIPSO) followed by CBES (1.7-fold higher than that of CDIPSO) and lowest for CDIPSO (Table S1). Such a pattern could be attributed to the fact that Bicine and BES have two ethoxy groups. However, Bicine has a carboxylic group linked by one carbon. In contrast, BES has a relatively bulky sulfonate group linked by two carbon atoms (Figure 1). Therefore, the spatial constraints on BES might have made it difficult to arrange and maximize the hydrogen bonding (H-bonding) and electrostatic interactions in similar environments. This might have resulted in decreased interactions of BES anion with other BES ions via H-bonding and thus the retention of choline cation, which prevents BES from holding more ionic motifs on the surface of PLGA and is responsible for the smaller CBES-NPs size as compared to CBicine-NPs. Similarly, the spatial considerations become more critical with the addition of another hydroxyl group in case of CDIPSO, which is structurally similar to CBES and thus leads to the smallest GBIL-NPs size among Group 1. In the case of CADA, CADA-NPs are relatively smaller in size than CBicine-NPs despite having a similar amount of CADA per NP (Table S1), which is ascribed to the efficient packing of di-anionic ADA ions with choline over PLGA surface (Figure 1).

Similarly, in Group 2, CTricine-NPs, CTES-NPs, and CTAPSO-NPs, which are greater compared to CACES-NPs, are likely due to more IL being present on each particle, evidenced by the corresponding amounts of these GBILs as 1.4-fold, 2.4-fold and 2-fold higher per NP of PLGA as compared to ACES (as determined by NMR measurements, Table S1).[50] Contrarily, CTAPS has 2.3-fold more IL per NP but is smaller than CACES-NPs. The greater size of CTricine, CTES, and CTAPSO NPs, unlike ACES NPs, is suggested to be due to the absence of hydroxyl groups in CACES IL (Figure 1). While for CTAPS, the efficient packing could lead to the concentration of a greater number of IL ions via H-bonding and electrostatic interactions over the PLGA NPs. Based on ring structure, Group 3 comprises three subtypes, i.e., piperazine (3a, HEPES, HEPBS, HEPPSO, and EPPS), cyclohexane (3b, CHES, CAPS, and CAPSO), and morpholine (3c, MES and MOPS). The size trend among piperazine analogs follows CHEPBS-NP > CHEPES-NP > CEPPS-NP ≈ CHEPPSO-NP. Similarly, cyclohexyl and morpholine analogues follow the size pattern CCHES-NP > CCAPS-NP > CCAPSO-NP and CMES-NP > CMOPS, respectively. Likewise, in Group 4 GBILs, CPOPOS-NPs are slightly greater than CPIPES-NPs. The quantitative NMR profile of these ILs indicates the presence of similar amounts of GBILs on PLGA NPs in their respective groups (Table S1). This leads to the fact that as in the case of groups 1 and 2, the relative extent of the size of cation/anion, packing efficiency, presence of functional groups (generating additional attractive interactions apart from ionic forces) along with their spatial orientation/location on cation/anion, determines the size and stability of the GBIL coating over PLGA NPs in case of group 3 and 4.

As discussed earlier, the interferences gained from the DLS measurements were very well correlated by proton NMR spectroscopy (^{1}H NMR, Table S1). The NMR data regarding all the GBIL NPs is provided in the supporting information, along with GBIL characterization. The NMR profile of CMES-NP (Figure 4), a representative of GBILs and GBIL NPs, shows that CMES has retained all of its proton peaks (except the peaks closest to the ring nitrogen, which get obscured by the PLGA (peak A, D Figure 4)) but gets shifted slightly downfield due to interactions at the PLGA surface and close proximity of the other ions in the nanoscale assembly. In CMES-NP, the cation/anion are present in a ratio 0.9: 1 (choline 3.19 (s, 13H) to MES 3.79 – 3.73 (m, 6H)). It was observed that all GBILs self-assemble over PLGA NPs in approximately 1:1 (Table S1) ratios irrespective of the molar ratio of their cation and anions that were added.

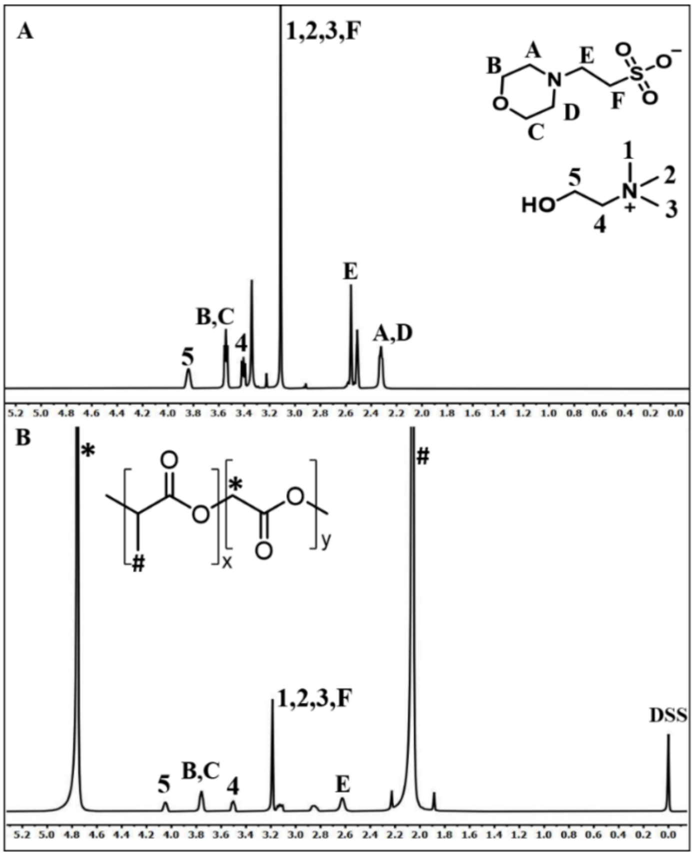

Figure 4. The successful coating of Good's buffer-based ionic liquids over PLGA nanoparticles using was confirmed by ^{1}H NMR spectroscopy. (A) ^{1}H NMR spectra of Choline MES 1:1 in DMSO; (B) Choline MES coated PLGA NPs containing 10 μL DSS (0.2 mg mL^{-1}) in D2O.

3.4. Interactions of GBIL-PLGA NPs in the biological microenvironment. To determine the biocompatibility of GBIL-PLGA NPs with the blood components, *ex vivo* serum adsorption with mouse and human serum was conducted using SDS-PAGE and LC-MS. Next, red blood cells (RBC) isolated from mouse and human blood were used to evaluate the hemolytic properties of GBILs-PLGA NPs. Last, cellular uptake of GBIL-PLGA NPs was performed with human triple-negative breast cancer cells (MDA-MB-231) and human normal healthy breast cells (MCF-10A).

3.4.1. Serum Protein Adsorption Liquid Chromatography-Tandem Mass Spectrometry (LC-MS/MS) Analysis. It is critical to consider how the GBILs influence the protein corona formation for intravenous drug delivery applications. Therefore, the affinity of different serum proteins towards GBIL-PLGA NPs was tested with freshly prepared NPs, treated with human and mouse serum separately in different experiments (see Method sections) and analyzed using SDS-PAGE and LC-MS. For both human and mouse serum, protein bands corresponding to different GBIL-NP samples look similar by SDS-PAGE (Figure 5A and B, Figure S3 and S4).

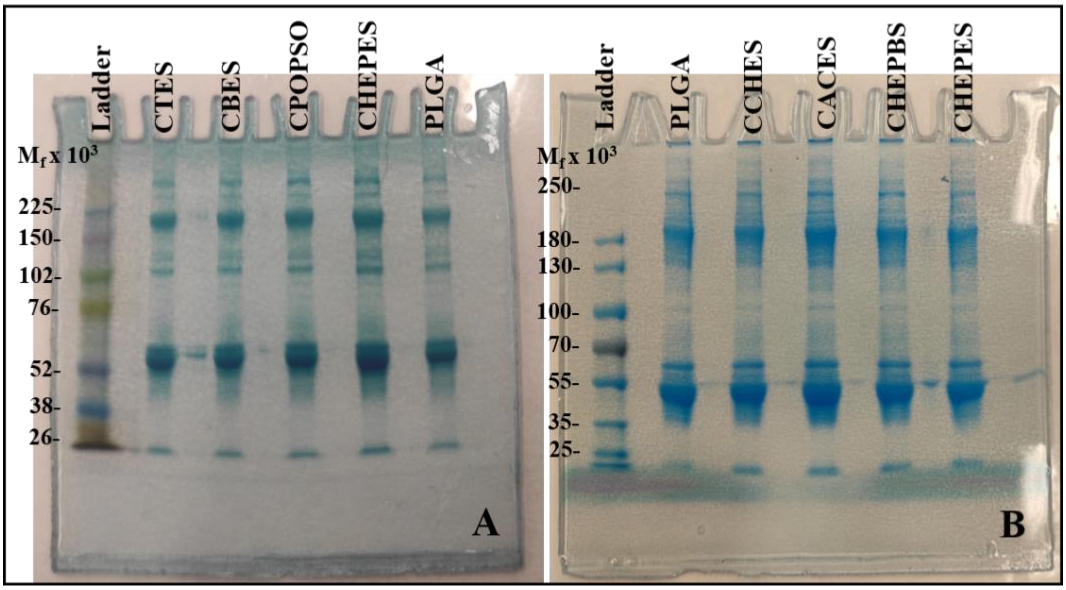

Figure 5. Serum protein adsorption profile of GBIL NPs in SDS-PAGE showing similar adsorption bands among different GBIL NPs. (A) Mouse and (B) Human serum protein adsorption, using 7.5% SDS-PAGE.

Therefore, in order to gain further insights, LC-MS studies were performed to identify different serum proteins present in the corona. The LC-MS data was analyzed based on absorption or depletion of specific protein onto the investigated NPs as compared to diluted serum as control. To calculate the relative intensity of a particular protein in a sample, the intensity of that protein was normalized by dividing it by the intensity of trypsin within the same sample, as well as the intensity of trypsin in the serum (positive control). Then, both values were divided and expressed in log base 10 to visualize fold-changes more easily. LC-MS/MS data for both human and mouse serum-treated GBIL-NPs was analyzed in comparison to serum and bare NPs to illustrate the variations in protein adsorption pre- and post-coating of GBIL compared to bare PLGA NPs (Figure 5 and 6). Due to complexity of system, all data for the GBIL-NPs is divided into 4 sets each with 5 GBILs and this grouping is slightly different than the Figure 1. Figure 5 and 6 demonstrates the differential protein adsorption patterns with and without GBIL-coating, while highlighting the type and extent of protein adsorption dependent on the GBIL-coating group 1.

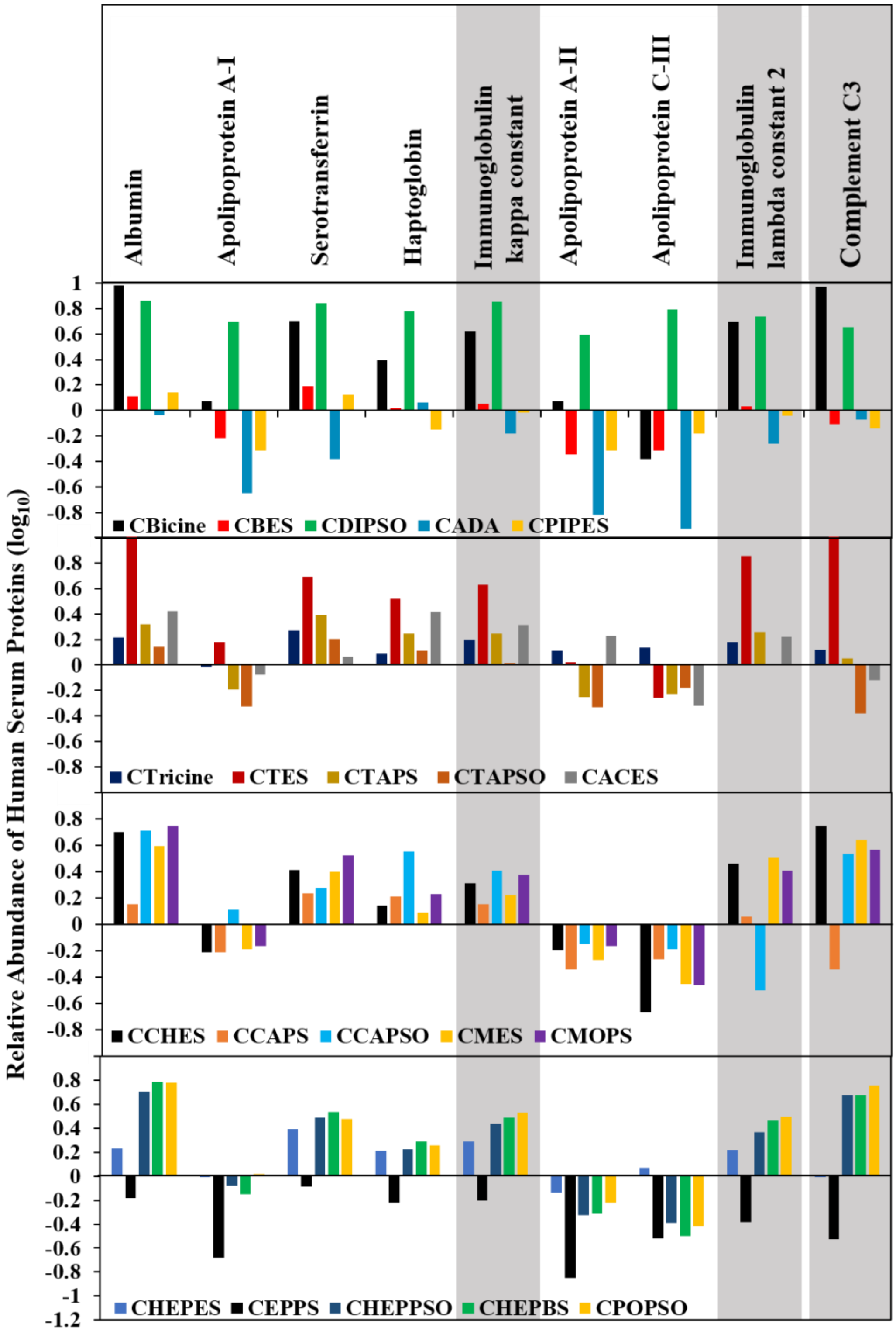

Figure 5. LC-MS profile showing relative adsorption and depletion of various human serum proteins depending on the chemical identity of GBIL-NPs. The intensity of the trypsin (used in the digestion of samples) was used to normalize the relative abundance of serum proteins adsorbed onto the bare and GBIL-coated PLGA nanoparticle surfaces; the final values were expressed as log10. Grey strips highlight the GBILs capable of reducing the adoption of immunoglobulins present in the serum which are responsible for the elimination of nanoparticles entering the blood stream.

In the case of human serum, out of 46 proteins (Table S2), 9 proteins were identified as common in all GBIL-NP samples, showing the variable extent of relative depletion/enrichment profile for GBIL-NPs compared to bare PLGA NPs. These proteins were found to play an essential role in various physiological processes in the human body, such as lipid metabolism (P02656, apolipoprotein C-III; P02652, apolipoprotein A-II; P02647, apolipoprotein A-I), immune function (P0DOY2, immunoglobulin lambda constant 2; P01834, immunoglobulin kappa constant; P01024, complement C3), iron transport (P02787, serotransferrin), and maintaining homeostasis (P00738, haptoglobin; P02768, albumin).

The specific binding preferences of these proteins for different GBIL-NPs are likely to have significant implications for their biological functions. For instance, in Group 1, CBicine-NP and CDIPSO-NP have exhibited the highest relative enrichment of identified common proteins on their surfaces, indicating their greater tendency to be eliminated by the immune system compared to bare PLGA-NPs due to increased absorption of immunoglobulins (Figure 5). Conversely, CBES-NPs have shown less depletion, while CADA-NPs have demonstrated greater relative depletion of proteins in Group 1. The variable depletion of all three immunoglobulins (P0DOY2, P01834, and P01024) found on the surface of CADA-NPs could make them more resilient toward the immune response compared to bare PLGA-NPs. Similarly, in other GBIL-subgroups, greater relative enrichment of almost all proteins identified as common was observed in CTES, CCAPSO, CHEPPSO, CHEPBS, and CPOPSO NPs. The relatively high affinity of immunoglobulins and lipid-binding protein for these NPs reflect the hydrophobic nature of these GBILs as compared to bare PLGA NPs and other GBILs and, therefore, more likely to elicit an immune response. In contrast, CTAPSO, CCAPS, CAPSO, and EPPS, due to their chemical structure and set of interactions, have shown depletion of these immunoglobulins and other proteins, and it was observed to be highest in EPPS NPs, suggesting its avoidance towards human immune proteins.

In the case of mouse serum, out of 72 proteins (Table S2), 13 proteins were identified as common in all GBIL samples. These proteins belong to various categories, such as carrier proteins (P07724, albumin), iron-binding proteins (Q921I1, serotransferrin), lipoproteins (Q00623, apolipoprotein A-I, and E, P08226), antibodies (P01837, immunoglobulin kappa constant; P01863, Ig gamma-2A chain C region A allele and A0A075B5P3, immunoglobulin heavy constant gamma 2B), protease inhibitors (P07759, serine protease inhibitor A3K), complement components (P01027, complement C3), and various other functional categories (Q91X72 Hemopexin; Q61646 Haptoglobin; Q61838 Pregnancy zone protein; A0A0R4J038 Bradykinin). The enrichment and depletion of GBIL-NPs in mouse serum have been evaluated in four different groups, labeled as groups 1 to 4 (Figure 6). Results indicate that groups 1 and 2 have demonstrated relatively high enrichment, while groups 3 and 4 have shown relatively high depletion compared to bare PLGA NPs. In group 1, CADA-NPs have displayed substantial relative depletion of immunoglobulins similar to that of human serum. Likewise, CTAPS-NPs have also prevented the adsorption of mouse immune proteins in group 2. In contrast, almost all GBIL-NPs in groups 3 and 4 have shown depletion of immunoproteins, with the exception of EPPS-NPs and CCAPSO-NPs, which have demonstrated moderate enrichment to slight depletion of these proteins. The study also revealed that the EPPS-NPs had the highest capacity for depleting human immunoglobulin. However, interestingly, they showed enrichment in mouse immunoglobulin. Additionally, in mouse serum, approximately 11 GBIL-NPs demonstrated relative depletion of immune proteins, compared to approximately 4 in human serum. These observations suggest that the interaction between immune proteins and GBIL-NPs is species-dependent, which underscores the evolutionary divergence of immune proteins and varying affinity for GBIL-NPs, despite their high similarity, and the importance of considering the choice of *ex vivo* models carefully.

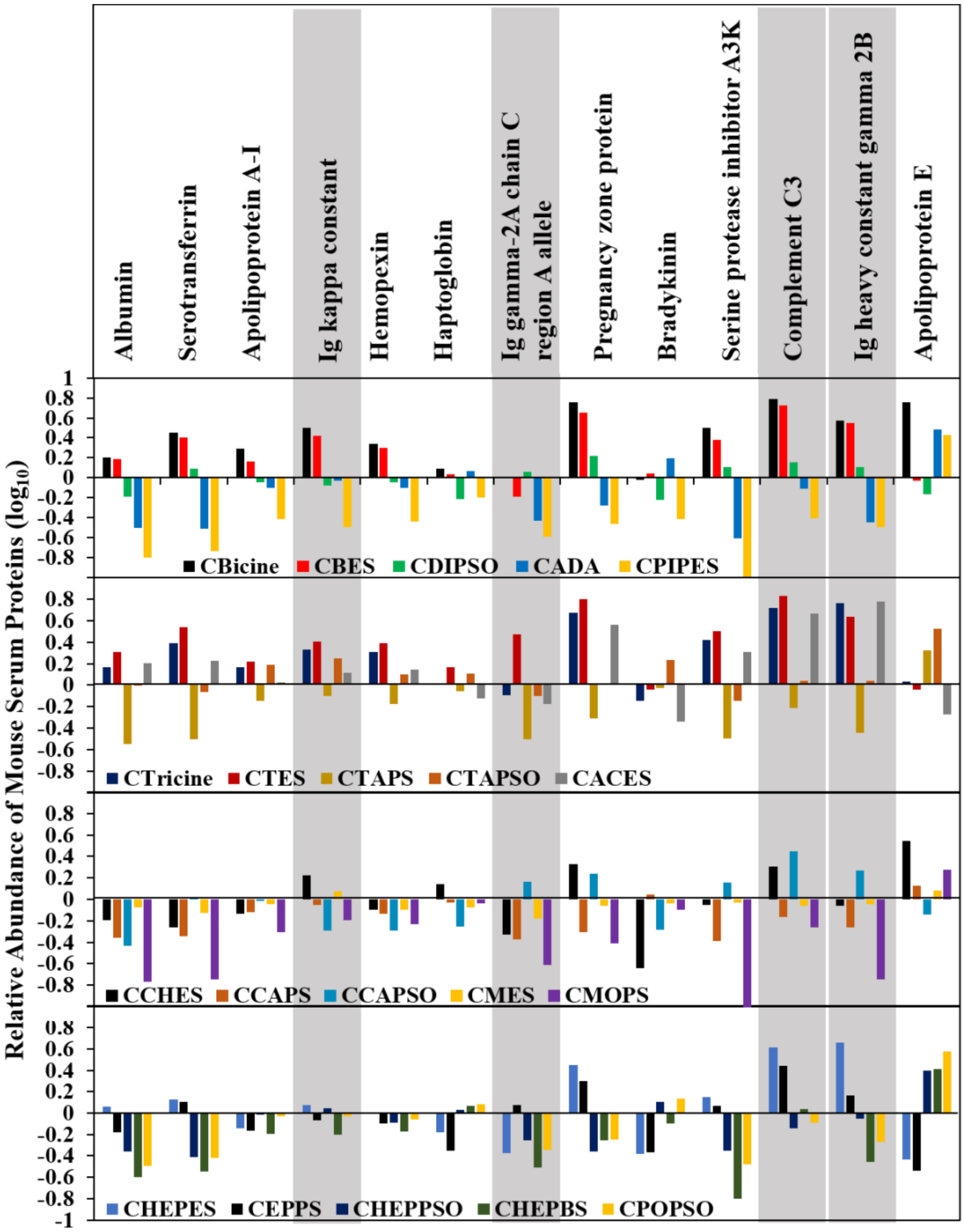

Figure 6. LC-MS profile showing relative adsorption and depletion of various mouse serum proteins depending on the nature of GBIL-NPs. The intensity of the trypsin (use in the digestion of samples) was used to normalize the relative abundance of serum proteins adsorbed onto the bare and GBIL-coated PLGA nanoparticle surfaces; the final values were expressed as log10. Grey strips highlight the GBILs capable of reducing the adoption of immunoglobulins present in the serum which are responsible for the elimination of nanoparticles entering the blood stream.

In the realm of nanoparticle-based drug delivery systems, the correlation between protein adsorption and their effectiveness in targeting cancer cells stands as a pivotal facet. The protein corona formation profoundly affects nanoparticle properties particularly in shaping their interactions with cells. Its composition varies based on nanoparticle surface properties and the biological environment. Here we observed that the GBIL-coated nanoparticles have reduced the immune-activating protein adsorption, which could potentially enhance their uptake by cancer cells. However, the relationship between protein adsorption and cancer cell targeting is complex, as some proteins may promote targeting while others hinder it. The specific proteins involved can vary depending on contextual factors and cell lines used, impacting nanoparticle behaviour and targeting efficiency.

3.4.2. Hemolysis. It is important to understand the nature of the interaction of GBIL-NPs with red blood cells (RBCs), which is the most abundant material in the blood after the plasma and serum. Adverse side reactions resulting in hemolysis (destruction of RBCs) could be fatal in some cases (depending upon dose size and clinical physiology)[51]. Therefore, to examine the extent of hemolysis induced by the GBIL-NPs, the synthesized GBIL-NPS were treated in three independent doses of 40:160, 20:180, and 10:190 of GBIL-NPs to the isolated RBCs of both human and mouse (BALB/c) in quadruplicate (n = 4) as mentioned in the previously reported protocol[18] (see Methods section). The rate of hemolysis in all cases i.e., with GBIL-PLGA NPs and bare PLGA NPs, was found to be below 10 % for both human and mouse RBCs (Figure 7).

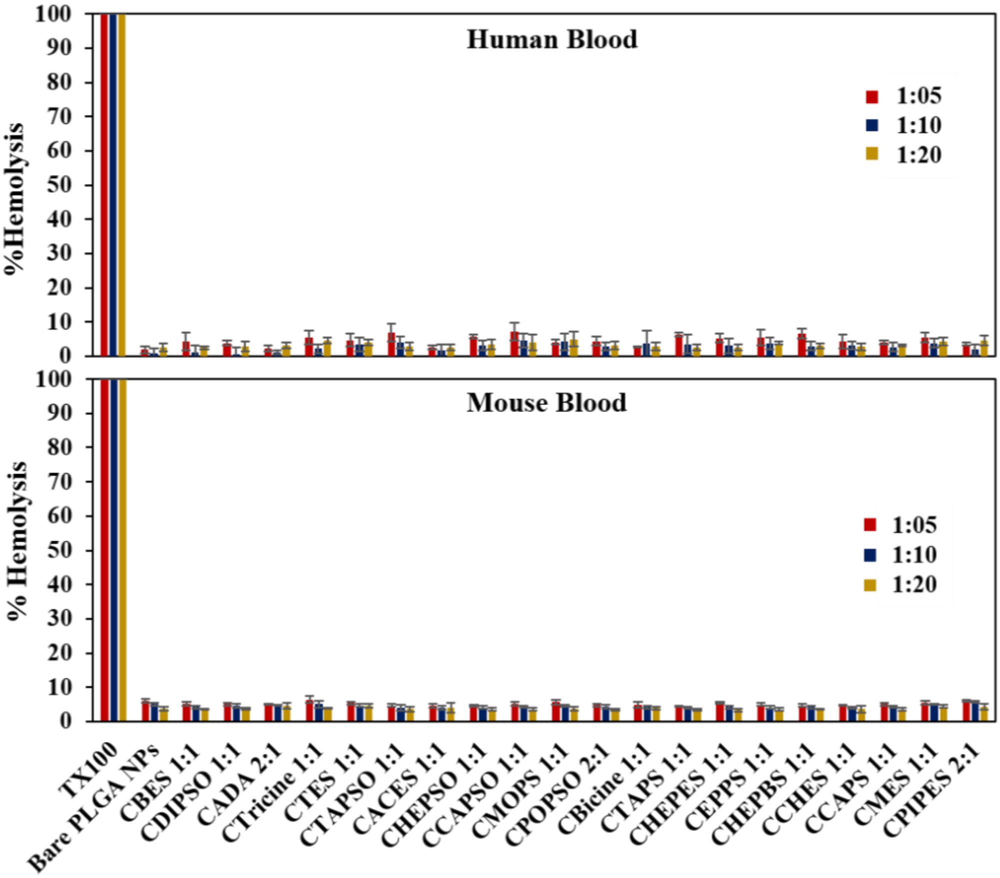

Figure 7. The GBIL-coated PLGA nanoparticles showing negligible hemolysis with human and mouse red blood cells (RBCs). The synthesized nanoparticles have shown an insignificant increase in hemolysis for both Human and Mouse RBCs compared to the control PLGA nanoparticles (n=4). Triton-X100 was used as a positive control.

This implies that the extent of hemolysis by GBIL-PLGA NPs is similar to PLGA NPs, which are known to cause insignificant hemolysis and FDA-approved polymer for *in vivo* applications and confirms the potential biocompatibility of GBIL-NPs and safety for intravenous (IV) delivery, although more thorough *in vivo* investigation is needed.

3.5. Cellular Uptake of GBIL-NPs by Cancer and Healthy Breast Cells. Cellular uptake of GBIL-PLGA NPs by human triple-negative breast cancer cell lines, (MDA-MB-231) and human healthy breast cell lines (MCF-10A) was conducted at concentrations of 10 μg mL^{-1}, 30 μg mL$^{-1,}$ and 50 μg mL^{-1} of NPs for 12 h, along with unmodified bare PLGA NPs as a control. The prepared samples were then analyzed by FACS (qualitative) and fluorescence plate reader (quantitative) measurements. In most cases, the uptake by each cell type was found to be higher as compared to unmodified bare PLGA NPs (Figure 8), indicating GBIL-directed more vital interaction of GBIL-PLGA NP interface with the cell membrane resulting in higher internalization of GBIL-coated NPs.

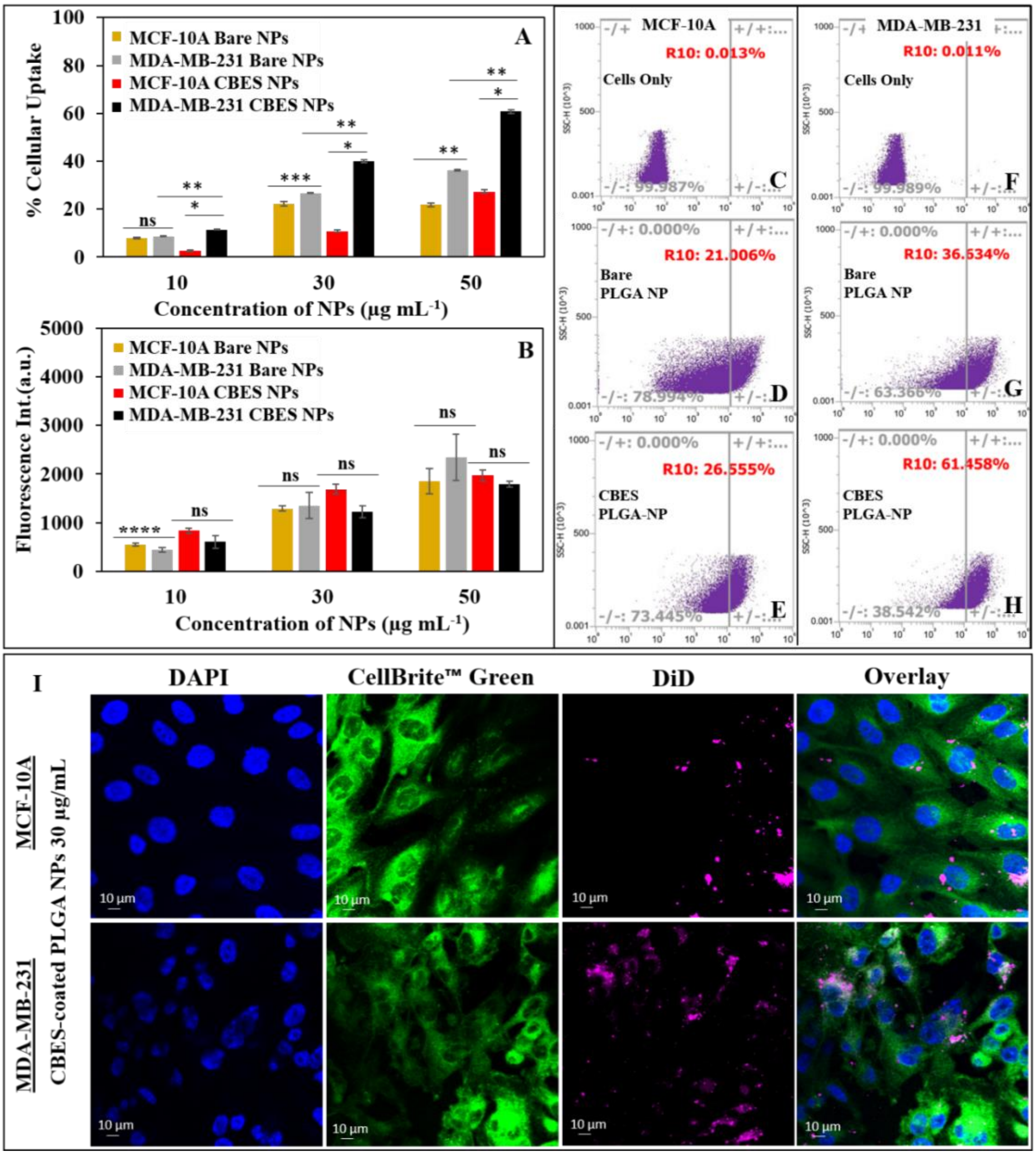

Figure 8. Selective uptake of GBIL-coated PLGA NPs by triple-negative breast cancer cells (MDA-MB-231). (A) Quantitative and (B) Qualitative investigation of DiD encapsulate good's buffer-coated PLGA nanoparticle cellular uptake by MCF-10A and MDA-MB-231 cells measured via fluorescent plate reader and FACS. FACS uptake by MCF-10A (C) Cells only (D) Bare PLGA NP at 50 µg mL^{-1} and (E) CBES-NP at 50 µg mL^{-1}; Uptake by MDA-MB-231 (F) Cells only (G) Bare PLGA NP at 50 µg mL^{-1}, (H) CBES-NP at 50 µg mL^{-1} (I) Confocal microscopy images of MCF-10A and MDA-MB-231 cells treated with 30 µg mL^{-1} CBES-coated PLGA DiD NPs at 37 ºC for 12 h, fixed, stained with DAPI (nuclei) and CellBrite™ Green (cytoplasmic membrane) and observed under 63× oil immersion lens; scale bar: 10 µm. * $p < 0.0001$, ** $p < 0.001$, ***$p < 0.005$, ****$p < 0.04$, ns-non-significant ($n = 3$).

Notably, 6 out of 20 GBILs resulted in preferential uptake of GBIL-NPs by MDA-MB-231 cells compared to healthy cells. The qualitative FACS profile of CBES-NPs demonstrated approximately a two-fold increase in uptake by MDA-MB-231 and a two-fold decrease in uptake by MCF-10A as compared to bare PLGA NPs (Figure 8A). Further, the extent of uptake was found to increase as a function of the concentration of CBES-NP dosage, confirming the selective accumulation of CBES-NPs into the MDA-MB-231 cells which is further evident by the confocal images (Figure 8I, Figure S6). On the other hand, measurement by fluorescence plate reader on the same cell samples showed similar cellular fluorescence for each sample, i.e., bare PLGA NPs and CBES-NPs in both MCF-10A and MDA-MB-231 cells (Figure 8B). In this context, the qualitative FACS data indicates that a higher proportion of MDA-MB-231 cells contain GBIL-NPs compared to MCF-10A cells (regardless of the number of NPs per cell). This observation contrasts with the quantitative fluorescence data, which measures the total number of NPs in all cells and suggests that the overall NP uptake may be similar between the two cell types.

Another GB anion, DIPSO, shares a structural resemblance with BES, differing only by one additional carbon and hydroxyl group. We observe that this change in chemistry results in CDIPSO-NPs showing preferential uptake into MCF-10A cells compared to MDA-MB-231 cells (Figure S5), suggesting that by manipulating the chemistry of the IL, we can control cellular uptake behavior. Another interesting example is CPOPSO and CPIPES, both of which are structurally similar 2:1 type ILs, and their anions differ only by one carbon and hydroxyl group on each side of piperazine ring (Figure 1). CPOPSO modified PLGA NPs demonstrated a two-fold selective uptake into MDA-MB-231 cells compared to MCF-10A. Contrarily, CPIPES-NPs showed selective uptake by MCF-10A compared to MDA-MB-231 cells (Figure S5).

Moreover, the cellular fluorescence quantitative data directly correlates to the uptake pattern obtained from FACS measurements, confirming the significant accumulation of CPOPSO-NPs in MDA-MB-231 cells. Likewise, four more GBIL were identified, namely, CADA, CACES, CTES, and CHEPBS, which were found to possess relatively selective uptake into MDA-MB-231 cells at higher concentrations of NPs but to a lesser degree compared to CBES and CPOPSO. The higher uptake of GBILs could be due to the resemblance of GBILs with the different biological substrates, which enable them to interact with cell receptors or charge-specific interactions with cell membranes[37,38] enabling them to modulate cell signaling. However, the mechanism of cellular uptake is complex, and it requires more research to establish the structure-function relationship between different GBIL-coatings and cell types.

4. Conclusions. Herein, we have reported 20 GBILs that show high biocompatibility and form stable coatings on PLGA NPs. All the tested GBIL-PLGA NPs were observed to be safe and stable in invitro biological environments as per *ex vivo* serum protein adsorption and hemolysis experiments. The investigated GBIL-PLGA NPs have shown structurally dependent preferential uptake into cancerous MDA-MB-231 cells compared to MCF-10A cells. Therefore, this works provides evidence that GBILs are promising surface coatings for polymeric nanoparticles and could be used to target specific cell types. Future work will focus on deepening our understanding of the underlying mechanism for the preferential uptake by specific cells by IL-polymer NPs, the delivery of active agents, and further assessment of safety profiles in vivo.

5. Acknowledgements.

EELT acknowledges the PhRMA Foundation, the College of Liberal Arts at the University of Mississippi, and the NSF CHE program for financial support. Research reported in this publication was supported by an Institutional Development Award (IDeA) from the National Institute of General Medical Sciences of the National Institutes of Health under award number P20GM130460.

References:

1. J. Ferlay, M. Colombet, I. Soerjomataram, D. M. Parkin, M. Piñeros, A. Znaor and F Bray, Cancer statistics for the year 2020: An overview, 2021, **149**, 778-789.
2. W. D. Foulkes, I. E. Smith and J. S. Reis-Filho, Triple-negative breast cancer, *N. Engl. J. Med.*, 2010, **363**, 1938-1948.
3. E. J. Dropcho, The neurologic side effects of chemotherapeutic agents, *CONTIN. Lifelong Learn. Neurol.*, 2011, **17**, 95-112.
4. R. R. Love, H. Leventhal, D. V. Easterling and D. R. J. C. Nerenz, Side effects and emotional distress during cancer chemotherapy, *Cancer*, 1989, **63**, 604-612.
5. D. M. Maino, S. Tran and F. Mehta, Side effects of chemotherapeutic oculo-toxic agents: a review, *Clin. Eye Vis. Care*, 2000, **12**, 113-117.
6. A. Umfress, H. E. Speed, C. Tan, S. Ramezani, S. Birnbaum, R. A. Brekken, X. Sun, F. Plattner, C. M. Powell and J. A. Bibb, Neuropathological effects of chemotherapeutic drugs, *ACS Chem. Neurosci.*, 2021, **12**, 3038-3048.
7. A. M. McCarthy, T. Friebel-Klingner, S. Ehsan, W. He, M. Welch, J. Chen, D. Kontos, S. M. Domchek, E. F. Conant and A. J. Semine, Relationship of established risk factors with breast cancer subtypes, *Cancer Med.*, 2021, **10**, 6456-6467.
8. N. Amreddy, A. Babu, R. Muralidharan, J. Panneerselvam, A. Srivastava, R. Ahmed, M. Mehta, A. Munshi and R. Ramesh, Recent advances in nanoparticle-based cancer drug and gene delivery, *Adv. Cancer Res.*, 2018, **137**, 115-170.
9. Y. Dang and J. Guan, Nanoparticle-based drug delivery systems for cancer therapy, *S.M.M.*, 2020, **1**, 10-19.
10. Y. Yao, Y. Zhou, L. Liu, Y. Xu, Q. Chen, Y. Wang, S. Wu, Y. Deng, J. Zhang and A. Shao, Nanoparticle-based drug delivery in cancer therapy and its role in overcoming drug resistance, *Front. Mol. Biosci.*, 2020, **7**, 193.
11. X. Yu, I. Trase, M. Ren, K. Duval, X. Guo and Z. J. Chen, Design of nanoparticle-based carriers for targeted drug delivery, *J. Nanomater.*, 2016.

12. K. Ulbrich, K. Holá, V. Šubr, A. Bakandritsos, J. Tuček and R. Zbořil, Targeted Drug Delivery with Polymers and Magnetic Nanoparticles: Covalent and Noncovalent Approaches, Release Control, and Clinical Studies, *Chemical Reviews*, 2016, **116**, 5338-5431.
13. X. Feng, F. Lv, L. Liu, H. Tang, C. Xing, Q. Yang and S. Wang, Conjugated Polymer Nanoparticles for Drug Delivery and Imaging, *ACS Applied Materials & Interfaces*, 2010, **2**, 2429-2435.
14. M. W. Tibbitt, J. E. Dahlman and R. Langer, Emerging Frontiers in Drug Delivery, *JACS*, 2016, **138**, 704-717.
15. H. Asem and E. Malmström, in *Gels and Other Soft Amorphous Solids*, American Chemical Society, 2018, vol. 1296, ch. 16, pp. 315-331.
16. M. Torrice, Does Nanomedicine Have a Delivery Problem?, *ACS Cent. Sci.*, 2016, **2**, 434-437.
17. J. Shi, P. W. Kantoff, R. Wooster and O. C. Farokhzad, Cancer nanomedicine: progress, challenges and opportunities, *Nat. Rev. Cancer.*, 2017, **17**, 20-37.
18. C. M. Hamadani, M. J. Goetz, S. Mitragotri and E. E. Tanner, Protein-avoidant ionic liquid (PAIL)–coated nanoparticles to increase bloodstream circulation and drive biodistribution, *Sci. Adv.*, 2020, **6**, eabd7563.
19. P. Wasserscheid and T. Welton, *Ionic liquids in synthesis*, Wiley Online Library, 2008.
20. R. Hayes, G. G. Warr and R. Atkin, Structure and Nanostructure in Ionic Liquids, *Chem. Rev.*, 2015, **115**, 6357-6426.
21. K. S. Egorova, E. G. Gordeev and V. P. Ananikov, Biological Activity of Ionic Liquids and Their Application in Pharmaceutics and Medicine, *Chem. Rev.*, 2017, **117**, 7132-7189.
22. R. F. Frade and C. A. Afonso, Impact of ionic liquids in environment and humans: an overview, *Hum. Exp. Toxicol.*, 2010, **29**, 1038-1054.
23. M. Amde, J.-F. Liu and L. Pang, Environmental application, fate, effects, and concerns of ionic liquids: a review, *Environ. Sci. Technol.*, 2015, **49**, 12611-12627.
24. E. E. Tanner, K. N. Ibsen and S. Mitragotri, Transdermal insulin delivery using choline-based ionic liquids (CAGE), *J. Control. Release*, 2018, **286**, 137-144.
25. E. E. Tanner, A. M. Curreri, J. P. Balkaran, N. C. Selig-Wober, A. B. Yang, C. Kendig, M. P. Fluhr, N. Kim and S. Mitragotri, Design principles of ionic liquids for transdermal drug delivery, *Adv. Mater.*, 2019, **31**, 1901103.
26. A. Vaidya and S. Mitragotri, Ionic liquid-mediated delivery of insulin to buccal mucosa, *J. Control. Release*, 2020, **327**, 26-34.
27. G. Singh, M. Kaur, D. Singh, A. K. Kesavan and T. S. Kang, Antimicrobial colloidal complexes of lysozyme with bio-based surface active ionic liquids in aqueous medium, *J. Phys. Chem. B.*, 2020, **124**, 3791-3800.
28. G. Singh, M. Kaur, H. Kaur and T. S. Kang, Synthesis and complexation of a new caffeine based surface active ionic liquid with lysozyme in aqueous medium: Physicochemical, computational and antimicrobial studies, *J. Mol. Liq.*, 2021, **325**, 115156.
29. M. Taha, M. R. Almeida, F. A. e. Silva, P. Domingues, S. P. Ventura, J. A. Coutinho and M. G. Freire, Novel biocompatible and self-buffering ionic liquids for biopharmaceutical applications, *Chem. Eur. J.*, 2015, **21**, 4781-4788.
30. N. E. Good, G. D. Winget, W. Winter, T. N. Connolly, S. Izawa and R. M. Singh, Hydrogen ion buffers for biological research, *Biochem.*, 1966, **5**, 467-477.
31. H. F. J. M. Zaki, Antioxidant and Antiinflammatory Effects of N-Hydroxyethylpiperazine-N-Ethanesulfonate (HEPES) in Adjuvant-Induced Arthritis, *MJPS*, 2008, **24**, 187-197.

32. N. A. Clark and J. E. Swain, Buffering systems in IVF, *CMSHART*, 2014, 30.
33. M. Petkovic, K. R. Seddon, L. P. N. Rebelo and C. S. Pereira, Ionic liquids: a pathway to environmental acceptability, *Chem. Soc. Rev.*, 2011, **40**, 1383-1403.
34. A. R. Jesus, L. R. Raposo, M. R. Soromenho, D. A. Agostinho, J. M. Esperança, P. V. Baptista, A. R. Fernandes and P. M. Reis, New non-toxic N-alkyl cholinium-based ionic liquids as excipients to improve the solubility of poorly water-soluble drugs, *Symmetry*, 2021, **13**, 2053.
35. J. Ranke, K. Mölter, F. Stock, U. Bottin-Weber, J. Poczobutt, J. Hoffmann, B. Ondruschka, J. Filser and B. Jastorff, Biological effects of imidazolium ionic liquids with varying chain lengths in acute Vibrio fischeri and WST-1 cell viability assays, *Ecotoxicol Environ Saf.*, 2004, **58**, 396-404.
36. P. Stepnowski, A. Skladanowski, A. Ludwiczak and E. J. H. Laczyńska, Evaluating the cytotoxicity of ionic liquids using human cell line HeLa, *Hum. Exp. Toxicol.*, 2004, **23**, 513-517.
37. S. Steudte, Investigations on the stability and ecotoxicity of selected ionic liquid cations and anions, 2014, Doctoral dissertation, Universität Bremen.
38. R. A. Kumar, N. Papaïconomou, J. M. Lee, J. Salminen, D. S. Clark and J. M. Prausnitz, In vitro cytotoxicities of ionic liquids: effect of cation rings, functional groups, and anions, *Environ. Toxicol.: Int. J.*, 2009, **24**, 388-395.
39. J. Ranke, M. Cox, A. Müller, C. Schmidt and D. Beyersmann, Sorption, cellular distribution, and cytotoxicity of imidazolium ionic liquids in mammalian cells–influence of lipophilicity, *Toxicol. Environ. Chem.*, 2006, **88**, 273-285.
40. D. J. Patinha, L. C. Tome, C. Florindo, H. R. Soares, A. S. Coroadinha, and I. M. Marrucho, New low-toxicity cholinium-based ionic liquids with perfluoroalkanoate anions for aqueous biphasic system implementation, *ACS Sustain. Chem. Eng.*, 2016, **4**, 2670-2679.
41. R. F. Frade, A. Matias, L. C. Branco, C. A. Afonso and C. M. Duarte, Effect of ionic liquids on human colon carcinoma HT-29 and CaCo-2 cell lines, *Green Chem.*, 2007, **9**, 873-877.
42. R. F. Frade, A. A. Rosatella, C. S. Marques, L. C. Branco, P. S. Kulkarni, N. M. Mateus, C. A. Afonso and C. M. Duarte, Toxicological evaluation on human colon carcinoma cell line (CaCo-2) of ionic liquids based on imidazolium, guanidinium, ammonium, phosphonium, pyridinium and pyrrolidinium cations, *Green Chem.*, 2009, **11**, 1660-1665.
43. G. Singh, M. Kaur, M. Singh, H. Kaur and T. S. Kang, Spontaneous Fibrillation of Bovine Serum Albumin at Physiological Temperatures Promoted by Hydrolysis-Prone Ionic Liquids, Langmuir, 2021, **37**, 10319-10329.
44. X.-D. Hou, Q.-P. Liu, T. J. Smith, N. Li and M.-H. Zong, Evaluation of toxicity and biodegradability of cholinium amino acids ionic liquids, *PLoS ONE*, 2013, **8**, e59145.
45. G. Singh, G. Singh and T. S. Kang, Effect of alkyl chain functionalization of ionic liquid surfactants on the complexation and self-assembling behavior of polyampholyte gelatin in aqueous medium, *Phys. Chem. Chem. Phys.*, 2016, **18**, 25993-26009.
46. G. Singh, G. Singh, S. Kancharla and T. S. Kang, Complexation behavior of β-lactoglobulin with surface active ionic liquids in aqueous solutions: An experimental and computational approach, *J. Phys. Chem. B.*, 2019, **123**, 2169-2181.
47. G. Singh, M. Kaur, V. K. Aswal and T. S. Kang, Aqueous colloidal systems of bovine serum albumin and functionalized surface active ionic liquids for material transport, *RSC Adv.*, 2020, **10**, 7073-7082.

48. M. Kaur, H. Kaur, M. Singh, G. Singh and T. S. Kang, Biamphiphilic ionic liquid based aqueous microemulsions as an efficient catalytic medium for cytochrome c, *Phys. Chem. Chem. Phys.*, 2021, **23**, 320-328.
49. C. M. Hamadani, I. Chandrasiri, M. L. Yaddehige, G. S. Dasanayake, I. Owolabi, A. Flynt, M. Hossain, L. Liberman, T. P. Lodge and T. A. Werfel, Improved nanoformulation and bio-functionalization of linear-dendritic block copolymers with biocompatible ionic liquids, *Nanoscale*, 2022, **14**, 6021-6036.
50. C.M. Hamadani, G. S. Dasanayake, M. E. Gorniak, M. C. Pride, W. Monroe, C. M. Chism, R. Heintz, E. Jarrett, G. Singh, S. X. Edgecomb, E. E. L. Tanner, Development of ionic liquid-coated PLGA nanoparticles for applications in intravenous drug delivery *Nat. Protoc.* 2023, **18**, 2509-2557.
51. W. Liu and D. Yu, Adverse drug reactions during ceftriaxone treatment can cause severe hemolysis, *Pediatr. Allergy Immunol.*, 2014, **1**, 101-102.